

# Characterizing the intrinsic properties of individual XFEL pulses via single-particle diffraction

Heemin Lee,<sup>a,‡</sup> Jaeyong Shin,<sup>a,‡</sup> Do Hyung Cho,<sup>a,‡</sup> Chulho Jung,<sup>a</sup> Daeho Sung,<sup>a</sup> Kangwoo Ahn,<sup>b</sup> Daewoong Nam,<sup>c</sup> Sangsoo Kim,<sup>c</sup> Kyung Sook Kim,<sup>c</sup> Sang-Yeon Park,<sup>c</sup> Jiadong Fan,<sup>d</sup> Huaidong Jiang,<sup>d</sup> Hyun Chol Kang,<sup>e</sup> Kensuke Tono,<sup>f</sup> Makina Yabashi,<sup>g</sup> Tetsuya Ishikawa,<sup>g</sup> Do Young Noh<sup>b</sup> and Changyong Song<sup>a,\*</sup>

Received 14 April 2019

Accepted 15 November 2019

Edited by M. Yamamoto, RIKEN SPring-8 Center, Japan

‡ These authors contributed equally to this work.

**Keywords:** X-ray free-electron lasers; single-particle diffraction; pulse energy; coherence; beam profile.

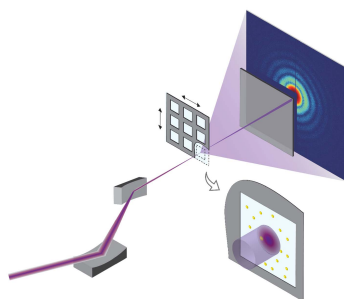
**Supporting information:** this article has supporting information at [journals.iucr.org/s](http://journals.iucr.org/s)

<sup>a</sup>Department of Physics, Pohang University of Science and Technology, Pohang 37673, South Korea, <sup>b</sup>Department of Physics and Photon Science, Gwangju Institute of Science and Technology, Gwangju 61005, South Korea, <sup>c</sup>PAL-XFEL Beamline Division, Pohang Accelerator Laboratory, Pohang 37673, South Korea, <sup>d</sup>School of Physical Science and Technology, ShanghaiTech University, Shanghai 201210, People's Republic of China, <sup>e</sup>Department of Materials Science and Engineering, Chosun University, Gwangju 61452, South Korea, <sup>f</sup>Japan Synchrotron Radiation Research Institute, 1-1-1 Kouto, Sayo, Hyogo 679-5198, Japan, and <sup>g</sup>RIKEN SPring-8 Center, 1-1-1 Kouto, Sayo, Hyogo 679-5148, Japan. \*Correspondence e-mail: [cysong@postech.ac.kr](mailto:cysong@postech.ac.kr)

With each single X-ray pulse having its own characteristics, understanding the individual property of each X-ray free-electron laser (XFEL) pulse is essential for its applications in probing and manipulating specimens as well as in diagnosing the lasing performance. Intensive research using XFEL radiation over the last several years has introduced techniques to characterize the femtosecond XFEL pulses, but a simple characterization scheme, while not requiring *ad hoc* assumptions, to address multiple aspects of XFEL radiation via a single data collection process is scant. Here, it is shown that single-particle diffraction patterns collected using single XFEL pulses can provide information about the incident photon flux and coherence property simultaneously, and the X-ray beam profile is inferred. The proposed scheme is highly adaptable to most experimental configurations, and will become an essential approach to understanding single X-ray pulses.

## 1. Introduction

Intense and coherent X-ray radiation with femtosecond (fs) pulse-width has become available with the advent of the X-ray free-electron lasers (XFELs) (Kang *et al.*, 2017; Milne *et al.*, 2017; Ishikawa *et al.*, 2012; Altarelli, 2011; Ackermann *et al.*, 2007; Emma *et al.*, 2010). By providing these new types of X-rays that have characteristics that are distinct from previously known types of electromagnetic radiation, the XFEL has enabled access to unexplored areas of science and technology. The data collection schemes with single femtosecond X-ray laser pulses have introduced new modalities to investigate specimens in environments that are close to their native conditions. Use of X-rays with fs pulse-width can avoid recording unwanted signals contaminated by sample damage caused by the absorption of X-ray energy during the measurements (Neutze *et al.*, 2000; Chapman *et al.*, 2014; Kimura *et al.*, 2014; Oroguchi & Nakasako, 2013). Intense radiation delivered in fs durations with a high degree of photon degeneracy has further invigorated research on the nonlinear interactions of X-rays with matter, to expand the exploitation of the quantum nature of X-rays (Tamasaku *et al.*, 2014; Young *et al.*, 2010; Singer *et al.*, 2013). The XFEL has facilitated applications in a wide range of research areas, and the interest to understand the very nature of XFEL radiation keeps increasing accordingly.



Radiation from XFELs, however, has a stochastic nature originating inherently from the peculiar lasing process of self-amplification spontaneous emission (SASE), and this makes each individual X-ray pulse unique (Saldin *et al.*, 1999). As such, characterizing XFEL radiation via single X-ray pulses is essential, and several types of experiment have been introduced to accomplish this task (Liu *et al.*, 2018; Nagler *et al.*, 2017; Sala *et al.*, 2017; Schropp *et al.*, 2013). Notwithstanding the successful demonstrations to measure the X-ray pulse energy (Tanaka *et al.*, 2017; Schneider *et al.*, 2018) and the coherence property (Gutt *et al.*, 2012; Jacques *et al.*, 2012; Vartanyants & Singer, 2010; Vartanyants *et al.*, 2011), often the characterizations of those properties have relied on independent experiments. This hinders us acquiring comprehensive information on individual X-ray pulses such as the correlation between coherence and total pulse energy delivered by the photons contained in a single-pulse wave packet.

Here we introduce a highly adaptable experimental scheme to characterize various physical properties of XFEL pulses from a single data-collection process. We have demonstrated that the single-shot coherent X-ray diffraction technique is a simple yet effective method to investigate both incident photon flux density and the coherence properties of each single X-ray pulse simultaneously. One can also estimate the average photon flux of the X-ray source and deduce the spatial beam profile from the analysis of the total pulse energy without additional instruments or separate experiments. Similar research has been introduced before to infer the pulse energy and beam profile (Daurer *et al.*, 2017; Loh *et al.*, 2013). Our approach, however, does not require *ad hoc* assumptions using standard nanoparticles as specimens and mounting them on flat membranes to allow precise investigation of the two-dimensional beam cross-section. This experiment is adaptable to most XFEL beamlines, and may have immediate applications in single-pulse characterizations. The results from two XFEL facilities – Pohang Accelerator Laboratory X-ray Free Electron Laser (PAL-XFEL) and SPring-8 Angstrom Compact X-ray free-electron Laser (SACLA) – are presented to demonstrate the adaptability and also the reliability of measurements.

## 2. Experiments

We have conducted single-pulse diffraction experiments both at BL3 of SACLA and the Nanocrystallography and Imaging (NCI) station at PAL-XFEL, and compared the characteristics of the two XFEL light sources. The experimental setup is the same as for those employed for single-pulse coherent diffraction imaging experiments in transmission geometry (Fig. 1). For both experiments, the X-ray energy was tuned to 5 keV without using a monochromator to take a natural energy bandwidth of  $\Delta E/E \simeq 0.3\%$  (Tono *et al.*, 2013). X-ray photons were delivered in pulses at a repetition rate of 10 Hz, and the pulse duration is shorter than 50 fs for SACLA and PAL-XFEL (Inubushi *et al.*, 2012). The X-ray beam was focused by a pair of Kirkpatrick–Baez mirrors manufactured by the same company (Yumoto *et al.*, 2013; Kim *et al.*, 2018).

The two beamlines have different focusing specifications to achieve  $1.5 \mu\text{m} \text{ (H)} \times 1.5 \mu\text{m} \text{ (V)}$  beam size at SACLA, and  $5 \mu\text{m} \text{ (H)} \times 5 \mu\text{m} \text{ (V)}$  at PAL-XFEL [full width at half-maximum (FWHM) values]. The size of the focused X-ray beam was measured by knife-edge scans using tungsten wires of diameter  $100 \mu\text{m}$ . The pointing stability of the focused X-ray beam was found to be smaller than the beam size. This positional fluctuation did not have a meaningful influence on this analysis.

The Multiple Application X-ray Imaging Chamber (MAXIC) (Song *et al.*, 2014) was used to record single-pulse coherent diffraction patterns at SACLA, and also a similarly designed chamber at PAL-XFEL. The intensity fluctuation of PAL-XFEL was smaller than 5% (Kang *et al.*, 2019), and this intensity variation was ignored in this analysis; the degree of sensitivity from the present analysis scheme is  $\sim 10\%$ , worse than this fluctuation.

Spherical Au nanoparticles of diameter 100 nm (Nanopartz Inc.) were used as specimens. Homogeneity of the nanoparticles in size and shape is important for the fidelity of the data analysis, and we have only used diffraction patterns from single nanoparticles of the same sizes and shapes in the analysis. Specimens were mounted using multiple-window  $\text{Si}_3\text{N}_4$  membranes with a membrane thickness of 100 nm (Silson Ltd). The single-pulse XFEL diffraction experiments were performed by raster scanning the sample stages with respect to the X-ray interaction spot (Park *et al.*, 2013; Nam *et al.*, 2016). The diffraction patterns were recorded by multiport readout charge coupled device (MPCCD) of pixel size  $50 \mu\text{m} \times 50 \mu\text{m}$  located 1.5 m downstream from the sample both at SACLA and PAL-XFEL (Kameshima *et al.*, 2014).

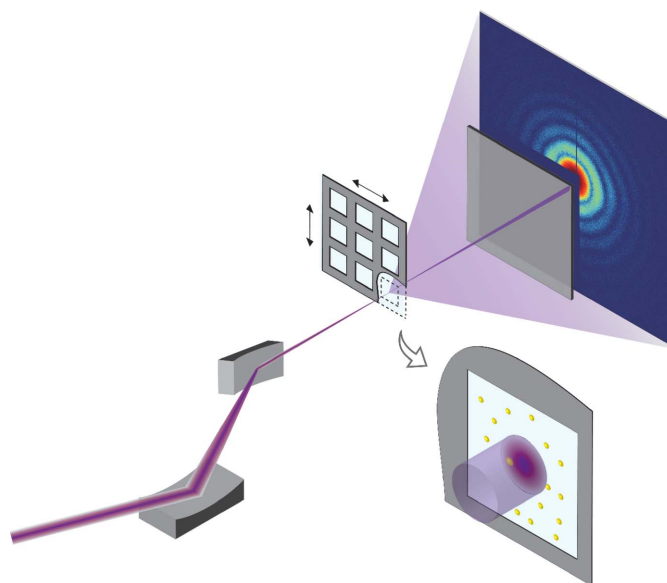


**Figure 1** XFEL pulse characterization using single-particle diffraction. Schematics of the single-particle diffraction experiments using focused single XFEL pulses employing the fixed target sample loading scheme are shown. Au nanospheres of diameter 100 nm are randomly located with respect to the focused XFEL beam with the intensity reflecting on the X-ray beam profile. Each single nanoparticle receives different photon flux depending on its location within the X-ray footprint.

### 3. Results and discussion

#### 3.1. X-ray pulse energy

Characterizing the total pulse energy of the XFEL is an important task not only for carrying out experiments but also for designing the optical components required for X-ray transportation while withstanding the heat load, for instance. With the large number of photons passing in an ultrashort pulse duration, measuring the pulse energy via conventional approach of either direct detection using photodiode, CCD detector or indirect monitoring via gas ionization becomes inaccurate. The X-ray pulse energy can also be implied by analyzing the back-scattered XFEL photons from amorphous material in a quadrant beam position monitor (QBPM) as often employed in various beamlines. However, quantitative measurements of the absolute X-ray pulse-energy require more elaborate calibrations. The absolute pulse energy of XFELs has been characterized through a thermodynamic method using a calibrated X-ray calorimetry (Tanaka *et al.*, 2017). The calorimetric measurements provide a quantitative estimation of the pulse energy with high accuracy ( $\sim 0.1\%$ ), but the available information is confined to average energy and the single pulse characterization is not a viable option yet.

Here, we employ single-particle diffraction to measure the incident photon flux density of single XFEL pulses. From the single-pulse diffraction of single particles, we can estimate the X-ray peak flux using the relation,  $I(Q) = I_0 r_e^2 N_e^2 |S_N(Q)|^2 \Delta^2 / z^2$ , with the detector having a finite pixel size ( $\Delta$ ) located at a distance  $z$  from the sample. The normalized structure factor  $S_N(Q)$  was employed reflecting the nanosphere of radius  $R$  as  $S(Q) \propto (4/3)\pi R^3 \Phi(QR)$ , with  $\Phi(x) = 3f(Q)[\sin(x) - x \cos(x)]/x^3$  (Kirz *et al.*, 1995; Shen *et al.*, 2004; Loh *et al.*, 2013). The momentum transfer between the incoming ( $\mathbf{k}_i$ ) and outgoing photon ( $\mathbf{k}_f$ ) is  $Q = |\mathbf{k}_f - \mathbf{k}_i|$ . The classical electron radius is denoted as  $r_e$ , and  $N_e$  gives the total number of electrons contained in the specimen. The atomic form factor,  $f(Q)$ , is taken as constant for the diffraction over the ultra-small angle ranges considered here, and similarly the polarization factor is also ignored. Often this relation is employed to calculate the mass density of the sample by knowing the incident photon flux ( $I_0$ ) (Gallagher-Jones *et al.*, 2014). Conversely, one can also estimate the incident flux using specimens with known mass, as done in the present analysis.

A single-pulse XFEL diffraction pattern of a spherical Au nanoparticle of diameter 100 nm was obtained [Fig. 2(a)]. The radial intensity was

obtained from the measured 2D speckle pattern after averaging over azimuthal angles, and the resulting intensity was fit to the expected structure factor of a solid sphere aforementioned [Fig. 2(b)]. In experiments, the diffraction intensity at the center ( $Q = 0$ ) was not directly measured. While blocking the direct XFEL beam with a piece of thick solid metal in front of the CCD detector to protect the CCD chip from intense radiation, the information delivering the diffraction intensity at the center was not measured directly. Instead, we obtained the intensity at  $Q = 0$  from the fit. The total electron number,  $N_e^2$ , was estimated for the standard Au nanoparticles. With these, we estimated the flux density of the incident X-ray ( $I_0$ ) impinging on the specimen. As the X-ray beam has a spatial variation in the intensity profile and the specimen is smaller than the beam size, estimated  $I_0$  denotes the flux density at the position of the specimen [ $I_0(r)$ ] with respect to the beam center (Fig. 1). The total flux is then estimated as  $I = \int_0^\infty I_0(r) 2\pi r dr$ .

We have considered the focused beam profile as a Gaussian shape. The stable beam condition of PAL-XFEL with a low-intensity fluctuation of less than 5% and a position stability of smaller than 10% of the beam size support our presumption of the Gaussian beam shape. The total flux of the X-ray photons contained in the Gaussian beam was extracted by knowing the maximum flux density at the center [ $I_0(r = 0)$ ] and the full width at half-maximum (FWHM) of the focused X-ray beam.

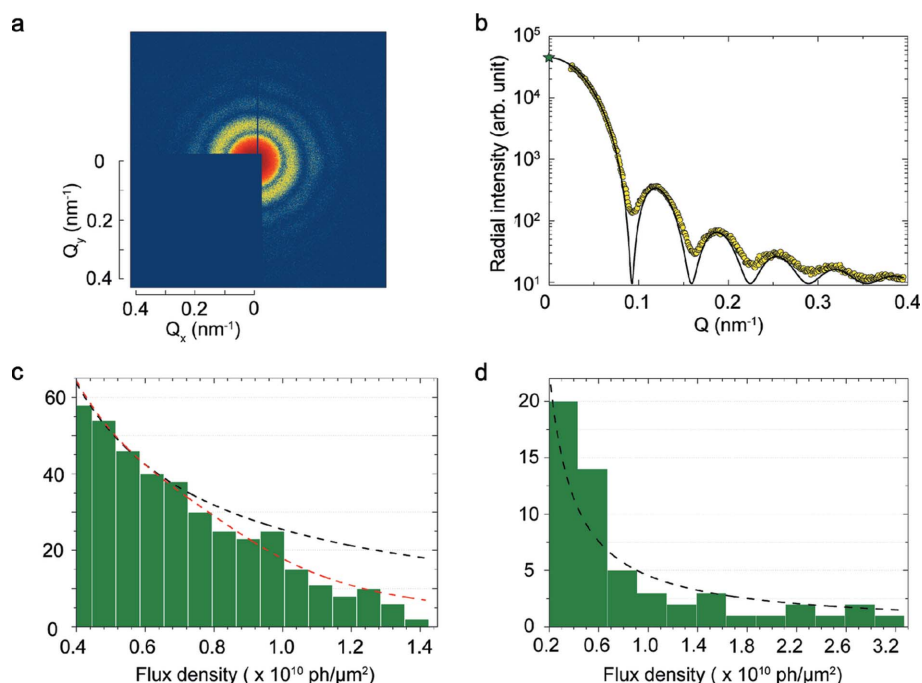


**Figure 2**

Characterizing the incident photon flux from diffraction intensities of single nanoparticles. (a) Single-pulse diffraction pattern measured using a spherical Au nanoparticle of diameter 100 nm. (b) The radial intensity (yellow circles) is fitted to the square of the form factor of an ideal sphere of the same size made of Au (solid line). (c) A histogram of incident flux densities,  $I_0(r_i)$ , estimated from 452 single-pulse diffraction patterns is drawn. The black dashed line represents the expected intensity distribution from a 2D Gaussian beam profile with a beam size of  $5 \mu\text{m} \times 5 \mu\text{m}$  FWHM. Best fit was obtained using a double-Gaussian beam profile with  $2 \mu\text{m} \times 2 \mu\text{m}$  and  $6 \mu\text{m} \times 6 \mu\text{m}$  beam sizes in a 4:1 intensity ratio (red dashed line). (d) An intensity histogram from 55 single-pulse diffraction patterns from SACLA is displayed with a single-Gaussian beam profile (dashed line).

To accommodate accurate estimation, we used the information on the focused X-ray beam size from a knife-edge measurement. The maximum photon flux density at the center of the incident X-ray beam was obtained using a statistical approach described as follows. First, the single-pulse diffraction patterns were taken from a single nanosphere located randomly in the X-ray beam. Then we plotted the measured  $I_0(r)$  as a histogram, which displayed the population density of the intensity distribution in the spatial profile of the X-rays at the focal plane. Diffraction patterns from multiple particles were discarded.

Considering the random position of the particle in the X-ray focal spot with a spatial profile of the flux distribution, the probability of the particle receiving the given flux density is related to the cross-sectional intensity profile of the incident X-ray beam. Therefore, the histogram plot of the intensity  $I_0(r)$  distribution represents the probability that the nanoparticle is located in the region of measured flux density. This occupation probability is proportional to the area of equal intensity equivalent to the X-ray beam profile. Eventually, by comparing this histogram with a beam profile, one can determine the maximum flux density at the center. After obtaining the two values [ $I_0(r=0)$  and FWHM], we can perform the integration and obtain the total flux, or the total pulse energy.

The accuracy of this histogram analysis requires acquisition of diffraction patterns from single particles sitting on a well defined single plane oriented perpendicular to the X-ray. This requisite was fulfilled using our fixed-target sample loading method. Any deviation of the sample hit location from the single plane implies three-dimensional probing of the XFEL beam intensities, which then requires a 3D model of a focused XFEL beam to estimate the flux and the 2D beam profile.

We used 452 single-pulse coherent diffraction patterns of single spherical nanoparticles collected at PAL-XFEL. The radial plot was obtained for each single particle diffraction pattern and fit to the structure factor to obtain  $I_0(r_i)$ . We then obtained the intensity histogram [Fig. 2(c)] using all  $I_0(r_i)$  with  $1 \leq i \leq 452$ . The intensity histogram was compared with a Gaussian beam profile. The dashed line in Fig. 2(c) shows a single Gaussian beam with maximum flux density  $I_0(r=0)$  of  $1.4 \times 10^{10}$  photons  $\mu\text{m}^{-2}$ . Using the intensity histogram of all 452 pulses, the total flux contained in a single pulse was estimated to be  $4.0 \times 10^{11}$  photons. This provided the average number of photons actually delivered to the interaction point where the specimens were loaded.

We refined this estimate by considering a beam composed of a double Gaussian [Fig. 2(c), red dashed line]. We found a decent fit to the histogram using a double Gaussian with widths of  $2 \mu\text{m} \times 2 \mu\text{m}$  and  $6 \mu\text{m} \times 6 \mu\text{m}$  and an intensity ratio of 4:1. Those values were also consistent with the measured beam size. The total flux estimated using the double Gaussian remained at a similar level of  $\sim 5.0 \times 10^{11}$  photons  $\mu\text{m}^{-2}$  showing that the estimated total flux was not too sensitive to a specific beam profile. The corresponding increase of the beam cross-section was  $\sim 23\%$  from the single to the double Gaussian distribution leading to increased total flux by  $\sim 25\%$ . Our choice of parameters was empirical, and the total flux esti-

mation did not show a keen dependence on it. The obtained X-ray pulse energy is consistent with the recent calorimetry measurements to be published elsewhere.

This histogram analysis is similar to X-ray footprint measurements performed using X-ray damage experiments on a polymer-coated surface or on Si wafers (Rösner *et al.*, 2017; Hau-Riege *et al.*, 2010). However, the histogram analysis of single-particle diffraction patterns proposed here promoted accurate estimation owing to the improved linearity of the X-ray flux to the signals, as the intensity distribution is obtained quantitatively.

We also note that the double Gaussian beam profile can be more consistent than the single Gaussian with its spatial coherence property. It is shown by the contributions of higher-order Gaussian modes as reported recently and the observation of interference from specimens separated by more than several micrometres. This result suggests that XFEL beam profiles can be acquired from the intensity histogram of the single-particle diffraction patterns.

Similar analysis was performed for the single-particle diffraction data collected at SACLA. We have filtered out collected data to use only single-particle diffraction patterns of the same size and shape. Diffraction patterns from multiple particles displayed interference fringes, which were also excluded. A total of 55 single-pulse diffraction patterns were used to obtain the intensity histogram [Fig. 2(d)]. A single Gaussian profile showed good agreement with the histogram [Fig. 2(d), dashed line]. A larger number of diffraction patterns would help to perform more accurate analysis, but the current estimation still provided reasonable estimation about the total flux. Overall, these results verify that the proposed scheme is appropriate to characterize the XFEL pulse energy, independent of experimental platforms.

### 3.2. Coherence property of micrometre-focused X-rays

The degree of spatial coherence is one of the important parameters to guide XFEL usage in many important applications including the single-particle 3D imaging (Song, 2018; Ekeberg *et al.*, 2015). It has often been characterized using Young's double-slit experiment, statistical speckle analysis and other methods (Vartanyants *et al.*, 2011; Lee *et al.*, 2013; Lehmkuhler *et al.*, 2014; Inoue *et al.*, 2015; Kobayashi *et al.*, 2018; Cho *et al.*, 2019). These experiments provide quantitative measures of the spatial coherence using well customized experimental configurations, but often those approaches are exclusive to the purposed experiment only.

Speckle visibility of diffraction patterns is directly related to the coherence, so the degree of spatial coherence can be estimated from single-particle diffraction patterns as follows. We incorporated the finite degree of coherence using the Gaussian Schell-model (GSM), for which the spatial degree of mutual coherence  $\mu(\Delta x, \Delta y)$  on the  $(x, y)$  plane is approximated as  $\mu(\Delta x, \Delta y) = \exp[-l^2/(2\sigma_\mu^2)]$ . Here,  $(\Delta x, \Delta y) = (x_1 - x_2, y_1 - y_2)$ , and  $\sigma_\mu$  is the spatial coherence length in the root-mean-square (RMS) value. The spatial separation of the photons impinging onto two separated points is considered

only for the relative distance between them as  $l = [(\Delta x)^2 + (\Delta y)^2]^{1/2}$ . The diffraction intensity, taking into account the finite degree of spatial coherence, is obtained from the Fourier transform (FT) as  $I(k_x, k_y) = \text{FT}\{A[\rho(x, y)]\mu(\Delta x, \Delta y)\}$  (Goodman, 2015). Here  $\rho(x, y)$  is the electron density projected along the plane perpendicular to the X-ray and  $A[\rho(x, y)]$  is the autocorrelation of the projected density map.

We have fit the radial intensity to a theoretical structure factor of a solid sphere, and have attributed the smearing of the oscillating fringe to a limited degree of spatial coherence in incoming X-rays [Fig. 3(a)]. The spatial coherence length was estimated for each single-pulse diffraction pattern using the relation above. The fringe visibility of the diffraction pattern may also be degraded caused by other experimental sources such as a finite pixel size of the detector to have unintended integration of X-rays over the detector pixel area, shot noise, parasitic scatterings from various components in the X-rays other than specimens *etc.* We have carefully controlled those sources. The high sampling rate was maintained to have more than 70 points for one fringe oscillation, with which the integration effect is avoided practically. The noise was filtered out by inspecting the distribution of CCD

counts. CCD counts of less than 20 were ignored with one X-ray photon producing  $\sim 88$  counts (see Fig. S1 of the supporting information).

The best fit to the data gave a spatial coherence length of  $1.16 \pm 0.07 \mu\text{m}$ . A comparison with different values of coherence lengths (0.6 and  $2.5 \mu\text{m}$ ) demonstrates the sensitivity of the spatial coherence on fringe visibility [Fig. 3(a)]. Single-pulse diffraction patterns of single nanospheres collected at SACLA were fit following the same procedure [Fig. 3(b)]. Here we used the results from 22 diffraction patterns out of 55 to maintain the fidelity of the estimation. Fitting the diffraction data with weak signals was often vulnerable to background noise that reduced the fit accuracy, so we filtered these out in the coherence analysis (see Fig. S2 of the supporting information). The average value of the spatial coherence length was  $0.94 \pm 0.11 \mu\text{m}$ , which agrees with the reported values from other experiments (Inoue *et al.*, 2015; Cho *et al.*, 2019).

We noticed a subtle dependence of coherence on pulse energy (see Fig. S3 of the supporting information). Additional investigation should be conducted to determine whether this correlation is real.

### 3.3. Temporal coherence

We use simulation to propose that the temporal coherence length can be deduced from the single-particle pattern if the signals are discernible at high enough momentum transfer values and the angular resolution of the detector is fine enough. The temporal coherence of the X-rays is determined by its spectral bandwidth as given by  $\xi_L \simeq \lambda^2/\Delta\lambda$ . This deviation in the wavelength, hence, would smear out the fringe oscillations along the longitudinal momentum transfer direction as

$$q_L = (4\pi/\lambda) \sin(2\theta/2) \simeq (2\pi/\lambda)(n\Delta/z), \quad (1)$$

where the diffraction angle between the incident and the diffracted X-ray beam is noted as  $2\theta$ , and  $n$  is the integer index in units of detector pixel size ( $\Delta$ ) from the direct X-ray beam position. The sample-to-detector distance is  $z$ .

The resolving power to distinguish such a spectral deviation ( $\delta\lambda$ ) depends on the available angular resolution of the detector employed, which is determined from the detector pixel resolution. Using equation (1), one can obtain

$$\left| \frac{\delta\lambda}{\lambda} \right| = \left| \frac{1}{\tan(2\theta/2)} \right| \delta \left( \frac{2\theta}{2} \right) = \left| \frac{1}{2 \tan(2\theta/2)} \right| \frac{p}{z}. \quad (2)$$

For a small diffraction angle [ $2 \tan(2\theta/2) \simeq Np/z$ ], the maximum spectral resolution becomes  $1/N$ , where  $N$  is the maximum number of detector pixels from the beam center. To assess the validity of this proposal, we numerically simulated the radial intensity distribution from the same spherical particle by considering the spectral broadening for a typical SASE bandwidth of  $\Delta E/E = 10^{-3}$  compared with  $\Delta E/E = 10^{-2}$  and  $\Delta E/E = 0$  (Fig. 4). The result suggests that the information on the degree of longitudinal coherence can be resolved if the detector has sufficiently fine angular resolution,

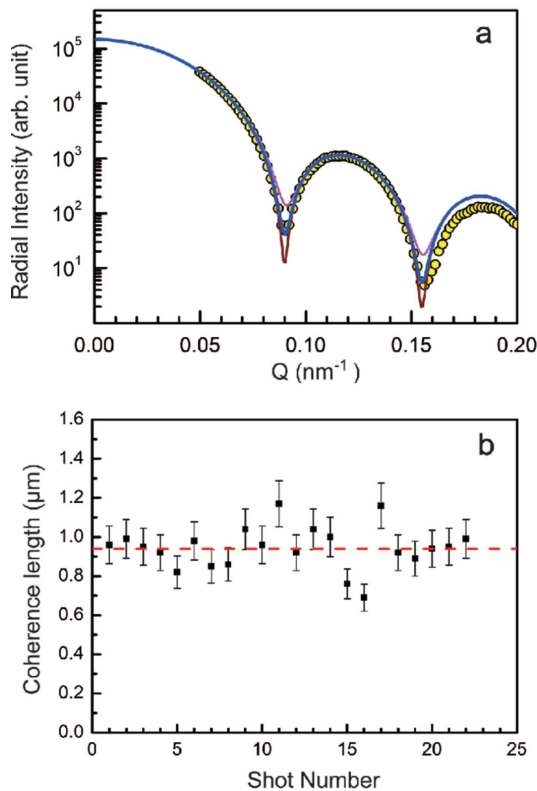


**Figure 3** Characterization of the spatial coherence. (a) The radial intensity is fit to the structure factor of an ideal sphere by incorporating the spatial coherence with details described in the text. Best fit to the data is obtained for the coherence length of  $1.16 \mu\text{m}$  (blue solid line). Others for the spatial coherence lengths of  $0.6 \mu\text{m}$  (magenta) and  $2.5 \mu\text{m}$  (dark brown) are compared. (b) The spatial coherence lengths for single X-ray pulses from SACLA are obtained. The average value was  $0.94 \pm 0.11 \mu\text{m}$  (red dashed line).

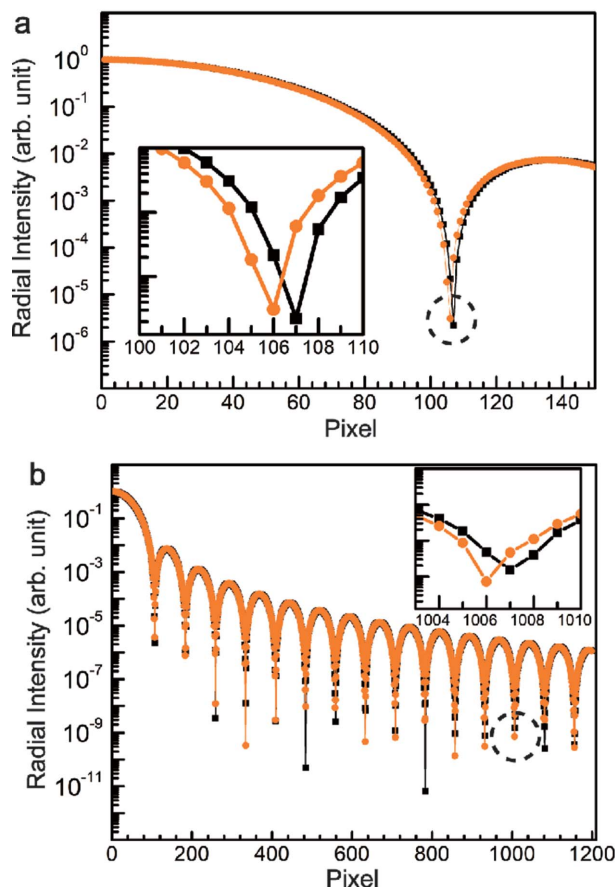


**Figure 4** Deviation in the fringe oscillation due to spectral broadening. Radial intensity is calculated for the 100 nm Au nanosphere, and the results are compared for different spectral bandwidths of  $\Delta E/E = 10^{-2}$  in (a) and  $\Delta E/E = 10^{-3}$  in (b) relative to  $\Delta E/E = 0$  (black solid line with square). The shift in the fringe oscillation period due to the spectral broadening becomes discernible after the  $m$ th pixel with  $m \simeq E/\Delta E$ .

which is related to the maximum diffraction angle and to the size of the detector pixel. For instance, in an ordinary detector that is composed of a mega-pixel array, a spectral distribution of  $10^{-3}$  results in a one-pixel shift in the fringe oscillation at the detector edge. This simulation assumes that the signal is clearly detectable out of the noise, which implies that the incident photon flux is high enough to sustain diffraction signal up to  $\sim 10^9$  scale. The bandwidth was not actually resolved in the present experiments hindered by weak diffraction signals.

#### 4. Summary

We have demonstrated that single-pulse coherent diffraction is a useful technique to probe the fundamental characteristics of individual X-ray pulses from free-electron lasers. Both the X-ray flux density and the degree of spatial coherence were estimated simultaneously from single-pulse diffraction patterns of single Au nanoparticles. Information on the X-ray beam profile was deduced by analyzing the intensity histogram. The feasibility to evaluate the temporal coherence of the radiation was demonstrated through numerical simula-

tions. This simultaneous characterization scheme enables us to gain insight into any correlation between the coherence and peak flux, which helps to diagnose the X-ray lasing efficiency. Implementation of this measurement scheme to any experimental stations of XFELs is straightforward, and we believe it will invigorate research that exploits utilizing the unique characteristics of XFELs.

#### Acknowledgements

We acknowledge the experimental support from SACLA technical support team, DAQ team, and staff scientists at PAL-XFEL. The XFEL experiments at SACLA (2012B8023, 2013A8028, 2013B8034, 2014A8020, 2014B8041, 2015B8031) were approved by Japan Synchrotron Radiation Research Institute and at PAL-XFEL by Korea Synchrotron Radiation Users Association (KOSUA) and funded by the Ministry of Science and ICT of Korea.

#### Funding information

Funding for this research was provided by: National Research Foundation of Korea (grant Nos. 2015R1A15A1009962; 2017K1A3A7A09016380; 2019R1A2B5B03070059); National Natural Science Foundation of China (grant No. 31430031 to JF, HJ).

#### References

Ackermann, W., Asova, G., Ayvazyan, V., Azima, A., Baboi, N., Bähr, J., Balandin, V., Beutner, B., Brandt, A., Bolzmann, A., Brinkmann, R., Brovko, O. I., Castellano, M., Castro, P., Catani, L., Chiadroni, E., Choroba, S., Cianchi, A., Costello, J. T., Cubaynes, D., Dardis, J., Decking, W., Delsim-Hashemi, H., Delsierieys, A., Di Pirro, G., Dohlus, M., Düsterer, S., Eckhardt, A., Edwards, H. T., Faatz, B., Feldhaus, J., Flöttmann, K., Frisch, J., Fröhlich, L., Garvey, T., Gensch, U., Gerth, C., Görler, M., Golubeva, N., Grabosch, H. J., Grecki, M., Grimm, O., Hacker, K., Hahn, U., Han, J. H., Honkavaara, K., Hott, T., Hüning, M., Ivanisenko, Y., Jaeschke, E., Jalmuzna, W., Jezynski, T., Kammering, R., Katalev, V., Kavanagh, K., Kennedy, E. T., Khodyachykh, S., Klöse, K., Kocharyan, V., Körfer, M., Kollwe, M., Koprek, W., Korepanov, S., Kostin, D., Krassilnikov, M., Kube, G., Kuhlmann, M., Lewis, C. L. S., Lilje, L., Limberg, T., Lipka, D., Löhl, F., Luna, H., Luong, M., Martins, M., Meyer, M., Michelato, P., Miltchev, V., Möller, W. D., Monaco, L., Müller, W. F. O., Napieralski, O., Napoly, O., Nicolosi, P., Nölle, D., Nuñez, T., Oppelt, A., Pagani, C., Paparella, R., Pchalek, N., Pedregosa-Gutierrez, J., Petersen, B., Petrosyan, B., Petrosyan, G., Petrosyan, L., Pflüger, J., Plönjes, E., Poletto, L., Pozniak, K., Prat, E., Proch, D., Pucyk, P., Radcliffe, P., Redlin, H., Rehlich, K., Richter, M., Roehrs, M., Roensch, J., Romaniuk, R., Ross, M., Rossbach, J., Rybnikov, V., Sachwitz, M., Saldini, E. L., Sandner, W., Schlarb, H., Schmidt, B., Schmitz, M., Schmüser, P., Schneider, J. R., Schneidmiller, E. A., Schnepf, S., Schreiber, S., Seidel, M., Sertore, D., Shabunov, A. V., Simon, C., Simrock, S., Sombrowski, E., Sorokin, A. A., Spanknebel, P., Spesyvtsev, R., Staykov, L., Steffen, B., Stephan, F., Stulle, F., Thom, H., Tiedtke, K., Tischer, M., Toleikis, S., Treusch, R., Trines, D., Tsakov, I., Vogel, E., Weiland, T., Weise, H., Wellhöfer, M., Wendt, M., Will, I., Winter, A., Wittenburg, K., Wurth, W., Yeates, P., Yurkov, M. V., Zagorodnov, I. & Zapfe, K. (2007). *Nat. Photon.* **1**, 336–342.

Altarelli, M. (2011). *Nucl. Instrum. Methods Phys. Res. B*, **269**, 2845–2849.

- Chapman, H. N., Caleman, C. & Timneanu, N. (2014). *Philos. Trans. R. Soc. B: Biol. Sci.* **369**, 1647.
- Cho, D., Yang, J., Kim, S., Nam, D., Park, J., Kim, S., Tono, K., Yabashi, M., Ishikawa, T. & Song, C. (2019). *Opt. Express*, **27**, 19573–19582.
- Daurer, B. J., Okamoto, K., Bielecki, J., Maia, F. R. N. C., Mühlhig, K., Seibert, M. M., Hantke, M. F., Nettelblad, C., Benner, W. H., Svenda, M., Timneanu, N., Ekeberg, T., Loh, N. D., Pietrini, A., Zani, A., Rath, A. D., Westphal, D., Kirian, R. A., Awel, S., Wiedorn, M. O., van der Schot, G., Carlsson, G. H., Hasse, D., Sellberg, J. A., Barty, A., Andreasson, J., Boutet, S., Williams, G., Koglin, J., Andersson, I., Hajdu, J. & Larsson, D. S. D. (2017). *IUCrJ*, **4**, 251–262.
- Ekeberg, T., Svenda, M., Abergel, C., Maia, F. R. N. C., Seltzer, V., Claverie, J.-M., Hantke, M., Jönsson, O., Nettelblad, C., van der Schot, G., Liang, M., DePonte, D. P., Barty, A., Seibert, M. M., Iwan, B., Andersson, I., Loh, N. D., Martin, A. V., Chapman, H., Bostedt, C., Bozek, J. D., Ferguson, K. R., Krzywinski, J., Epp, S. W., Rolles, D., Rudenko, A., Hartmann, R., Kimmel, N. & Hajdu, J. (2015). *Phys. Rev. Lett.* **114**, 098102.
- Emma, P., Akre, R., Arthur, R., Bionta, R., Bostedt, C., Bozek, J., Brachmann, A., Bucksbaum, P., Coffee, R., Decker, F.-J., Ding, Y., Dowell, D., Edstrom, S., Fisher, A., Frisch, J., Gilevich, S., Hastings, J., Hays, G., Hering, P., Huang, Z., Iverson, R., Loos, H., Messerschmidt, M., Miahnahri, A., Moeller, S., Nuhn, H., Pile, G., Ratner, D., Rzepiela, J., Schultz, D., Smith, T., Stefan, P., Tompkins, H., Turner, J., Welch, J., White, W., Wu, J., Yocky, G. & Galayda, J. (2010). *Nat. Photon.* **4**, 641–647.
- Gallagher-Jones, M., Bessho, Y., Kim, S., Park, J., Kim, S., Nam, D., Kim, C., Kim, Y., Noh, D. Y., do, Y., Miyashita, O., Tama, F., Joti, Y., Kameshima, T., Hatsui, T., Tono, K., Kohmura, Y., Yabashi, M., Hasnain, S. S., Ishikawa, T. & Song, C. (2014). *Nat. Commun.* **5**, 3798.
- Goodman, J. W. (2015). *Statistical Optics*, 2nd ed. Hoboken: John Wiley & Sons Inc.
- Gutt, C., Wochner, P., Fischer, B., Conrad, H., Castro-Colin, M., Lee, S., Lehmkuhler, F., Steinke, I., Sprung, M., Roseker, W., Zhu, D., Lemke, H., Bogle, S., Fuoss, P. H., Stephenson, G. B., Cammarata, M., Fritz, D. M., Robert, A. & Grübel, G. (2012). *Phys. Rev. Lett.* **108**, 024801.
- Hau-Riege, S. P., London, R. A., Graf, A., Baker, S. L., Soufli, R., Sobierajski, R., Burian, T., Chalupsky, J., Juha, L., Gaudin, J., Krzywinski, J., Moeller, S., Messerschmidt, M., Bozek, J. & Bostedt, C. (2010). *Opt. Express*, **18**, 23933–23938.
- Inoue, I., Tono, K., Joti, Y., Kameshima, T., Ogawa, K., Shinohara, Y., Amemiya, Y. & Yabashi, M. (2015). *IUCrJ*, **2**, 620–626.
- Inubushi, Y., Tono, K., Togashi, T., Sato, T., Hatsui, T., Kameshima, T., Togawa, K., Hara, T., Tanaka, T., Tanaka, H., Ishikawa, T. & Yabashi, M. (2012). *Phys. Rev. Lett.* **109**, 144801.
- Ishikawa, T., Aoyagi, H., Asaka, T., Asano, Y., Azumi, N., Bizen, T., Ego, H., Fukami, K., Fukui, T., Furukawa, Y., Goto, S., Hanaki, H., Hara, T., Hasegawa, T., Hatsui, T., Higashiya, A., Hirono, T., Hosoda, N., Ishii, M., Inagaki, T., Inubushi, Y., Itoga, T., Joti, Y., Kago, M., Kameshima, T., Kimura, H., Kirihara, Y., Kiyomichi, A., Kobayashi, T., Kondo, C., Kudo, T., Maesaka, H., Maréchal, X. M., Masuda, T., Matsubara, S., Matsumoto, T., Matsushita, T., Matsui, S., Nagasono, M., Nariyama, N., Ohashi, H., Ohata, T., Ohshima, T., Ono, S., Otake, Y., Saji, C., Sakurai, T., Sato, T., Sawada, K., Seike, T., Shirasawa, K., Sugimoto, T., Suzuki, S., Takahashi, S., Takebe, H., Takeshita, K., Tamasaku, K., Tanaka, H., Tanaka, R., Tanaka, T., Togashi, T., Togawa, K., Tokuhisa, A., Tomizawa, H., Tono, K., Wu, S., Yabashi, M., Yamaga, M., Yamashita, A., Yanagida, K., Zhang, C., Shintake, T., Kitamura, H. & Kumagai, N. (2012). *Nat. Photon.* **6**, 540–544.
- Jacques, V., Le Bolloc'h, D., Pinsolle, E., Picca, F.-E. & Ravy, S. (2012). *Phys. Rev. B*, **86**, 144117.
- Kameshima, T., Ono, S., Kudo, T., Ozaki, K., Kirihara, Y., Kobayashi, K., Inubushi, Y., Yabashi, M., Horigome, T., Holland, A., Holland, K., Burt, D., Murao, H. & Hatsui, T. (2014). *Rev. Sci. Instrum.* **85**, 033110.
- Kang, H.-S., Min, C.-K., Heo, H., Kim, C., Yang, H., Kim, G., Nam, I., Baek, S. Y., Choi, H.-J., Mun, G., Park, B. R., Suh, Y. J., Shin, D. C., Hu, J., Hong, J., Jung, S., Kim, S.-H., Kim, K., Na, D., Park, S. S., Park, Y. J., Han, J.-H., Jung, Y. G., Jeong, S. H., Lee, H. G., Lee, S., Lee, S., Lee, W.-W., Oh, B., Suh, H. S., Parc, Y. W., Park, S.-J., Kim, M. H., Jung, N.-S., Kim, Y.-C., Lee, M.-S., Lee, B.-H., Sung, C.-W., Mok, I.-S., Yang, J.-M., Lee, C.-S., Shin, H., Kim, J. H., Kim, Y., Lee, J. H., Park, S.-Y., Kim, J., Park, J., Eom, I., Rah, S., Kim, S., Nam, K. H., Park, J., Park, J., Kim, S., Kwon, S., Park, S. H., Kim, K. S., Hyun, H., Kim, S. N., Kim, S., Hwang, S., Kim, M. J., Lim, C., Yu, C., Kim, B., Kang, T., Kim, K., Kim, S., Lee, H., Lee, H., Park, K., Koo, T., Kim, D. & Ko, I. S. (2017). *Nat. Photon.* **11**, 708–713.
- Kang, H.-S., Yang, H., Kim, G., Heo, H., Nam, I., Min, C.-K., Kim, C., Baek, S. Y., Choi, H.-J., Mun, G., Park, B. R., Suh, Y. J., Shin, D. C., Hu, J., Hong, J., Jung, S., Kim, S.-H., Kim, K., Na, D., Park, S. S., Park, Y. J., Han, J.-H., Jung, Y. G., Jeong, S. H., Kim, M. J., Lee, H. G., Lee, S., Lee, W.-W., Oh, B., Suh, H. S., Park, K.-H., Lee, H.-S., Khan, D. Z., Raubenheimer, T. O. & Wu, J. (2019). *J. Synchrotron Rad.* **26**, 1127–1138.
- Kim, J., Kim, H.-Y., Park, J., Kim, S., Kim, S., Rah, S., Lim, J. & Nam, K. H. (2018). *J. Synchrotron Rad.* **25**, 289–292.
- Kimura, T., Joti, Y., Shibuya, A., Song, C., Kim, S., Tono, K., Yabashi, M., Tamakoshi, M., Moriya, T., Oshima, T., Ishikawa, T., Bessho, Y. & Nishino, Y. (2014). *Nat. Commun.* **5**, 3052.
- Kirz, J., Jacobsen, C. & Howells, M. (1995). *Q. Rev. Biophys.* **28**, 33–130.
- Kobayashi, A., Sekiguchi, Y., Oroguchi, T., Yamamoto, M. & Nakasako, M. (2018). *Sci. Rep.* **8**, 831.
- Lee, S., Roseker, W., Gutt, C., Fischer, B., Conrad, H., Lehmkuhler, F., Steinke, I., Zhu, D., Lemke, H., Cammarata, M., Fritz, D. M., Wochner, P., Castro-Colin, M., Hruszkewycz, S. O., Fuoss, P. H., Stephenson, G. B., Grübel, G. & Robert, A. (2013). *Opt. Express*, **21**, 24647–24664.
- Lehmkuhler, F., Gutt, C., Fischer, B., Schroer, M. A., Sikorski, M., Song, S., Roseker, W., Glowina, J., Chollet, M., Nelson, S., Tono, K., Katayama, T., Yabashi, M., Ishikawa, T., Robert, A. & Grübel, G. (2014). *Sci. Rep.* **4**, 5234.
- Liu, Y., Seaberg, M., Zhu, D., Krzywinski, J., Seiboth, F., Hardin, C., Cocco, D., Aquila, A., Nagler, B. & Lee, H. J. (2018). *Optica*, **5**, 967–975.
- Loh, N. D., Starodub, D., Lomb, L., Hampton, C. Y., Martin, A. V., Sierra, R. G., Barty, A., Aquila, A., Schulz, J., Steinbrener, J., Shoeman, R. L., Kassemeyer, S., Bostedt, C., Bozek, J., Epp, S. W., Erk, B., Hartmann, R., Rolles, D., Rudenko, A., Rudek, B., Foucar, L., Kimmel, N., Weidenspointner, G., Hauser, G., Holl, P., Pedersoli, E., Liang, M., Hunter, M. S., Gumprecht, L., Coppola, N., Wunderer, C., Graafsma, H., Maia, F. R. N. C., Ekeberg, T., Hantke, M., Fleckenstein, H., Hirsemann, H., Nass, K., White, T. A., Tobias, H. J., Farquar, G. R., Benner, W. H., Hau-Riege, S., Reich, C., Hartmann, A., Soltau, H., Marchesini, S., Bajt, S., Barthelmeß, M., Strueder, L., Ullrich, J., Bucksbaum, P., Frank, M., Schlichting, I., Chapman, H. N. & Bogan, M. J. (2013). *Opt. Express*, **21**, 12385–12394.
- Milne, C., Schietinger, T., Aiba, M., Alarcon, A., Alex, J., Anghel, A., Arsov, V., Beard, C., Beaud, P., Bettoni, S., Bopp, M., Brands, H., Brönnimann, M., Brunnenkant, I., Calvi, M., Citterio, A., Craievich, P., Csatari Divall, M., Dällenbach, M., D'Amico, M., Dax, A., Deng, Y., Dietrich, A., Dinapoli, R., Divall, E., Dordevic, S., Ebner, S., Erny, C., Fitze, H., Flechsig, U., Follath, R., Frei, F., Gärtner, F., Ganter, R., Garvey, T., Geng, Z., Gorgisyan, I., Gough, C., Hauff, A., Hauri, C., Hiller, N., Humar, T., Hunziker, S., Ingold, G., Ischebeck, R., Janousch, M., Juranić, P., Jurcevic, M., Kaiser, M., Kalantari, B., Kalt, R., Keil, B., Kittel, C., Knopp, G., Koprek, W., Lemke, H., Lippuner, T., Llorente Sancho, D., Löhl, F., Lopez-Cuenca, C., Märki, F., Marcellini, F., Marinkovic, G., Martiel, I.,

- Menzel, R., Mozzanica, A., Nass, K., Orlandi, G., Ozkan Loch, C., Panepucci, E., Paraliiev, M., Patterson, B., Pedrini, B., Pedrozzi, M., Pollet, P., Pradervand, C., Prat, E., Radi, P., Raguin, J., Redford, S., Rehanek, J., Réhault, J., Reiche, S., Ringele, M., Rittmann, J., Rivkin, L., Romann, A., Ruat, M., Ruder, C., Sala, L., Schebacher, L., Schilcher, T., Schlott, V., Schmidt, T., Schmitt, B., Shi, X., Stadler, M., Stingelin, L., Sturzenegger, W., Szlachetko, J., Thattil, D., Treyer, D., Trisorio, A., Tron, W., Vetter, S., Vicario, C., Voulot, D., Wang, M., Zamofing, T., Zellweger, C., Zennaro, R., Zimoch, E., Abela, R., Patthey, L. & Braun, H. (2017). *Appl. Sci.* **7**, 720.
- Nagler, B., Aquila, A., Boutet, S., Galtier, E. C., Hashim, A., Hunter, M. S., Liang, M., Sakdinawat, A. E., Schroer, C. G., Schropp, A., Seaberg, M. H., Seiboth, F., van Driel, T., Xing, Z., Liu, Y. & Lee, H. J. (2017). *Sci. Rep.* **7**, 13698.
- Nam, D., Kim, C., Kim, Y., Ebisu, T., Gallagher-Jones, M., Park, J., Kim, S., Kim, S., Tono, K., Noh, D. Y., Yabashi, M., Ishikawa, T. & Song, C. (2016). *J. Phys. B At. Mol. Opt. Phys.* **49**, 034008.
- Neutze, R., Wouts, R., van der Spoel, D., Weckert, E. & Hajdu, J. (2000). *Nature*, **406**, 752–757.
- Oroguchi, T. & Nakasako, M. (2013). *Phys. Rev. E*, **87**, 022712.
- Park, J., Joti, Y., Ishikawa, T. & Song, C. (2013). *Appl. Phys. Lett.* **103**, 264101.
- Rösner, B., Döring, F., Ribič, P. R., Gauthier, D., Principi, E., Masciovecchio, C., Zangrando, M., Vila-Comamala, J., De Ninno, G. & David, C. (2017). *Opt. Express*, **25**, 30686–30695.
- Sala, S., Daurer, B., Hantke, M., Ekeberg, T., Loh, N., Maia, F. R. & Thibault, P. (2017). *J. Phys. Conf. Ser.* **849**, 012032.
- Saldin, E. L., Schneidmiller, E. A. & Yurkov, M. V. (1999). *The Physics of Free Electron Lasers*. Berlin: Springer Verlag.
- Schneider, M., Günther, C. M., Pfau, B., Capotondi, F., Manfreda, M., Zangrando, M., Mahne, N., Raimondi, L., Pedersoli, E., Naumenko, D. & Eisebitt, S. (2018). *Nat. Commun.* **9**, 214.
- Schropp, A., Hoppe, R., Meier, V., Patommel, J., Seiboth, F., Lee, H. J., Nagler, B., Galtier, E. C., Arnold, B., Zastra, U., Hastings, J. B., Nilsson, D., Uhlén, F., Vogt, U., Hertz, H. M. & Schroer, C. G. (2013). *Sci. Rep.* **3**, 1633.
- Shen, Q., Bazarov, I. & Thibault, P. (2004). *J. Synchrotron Rad.* **11**, 432–438.
- Singer, A., Lorenz, U., Sorgenfrei, F., Gerasimova, N., Gulden, J., Yefanov, O. M., Kurta, R. P., Shabalin, A., Dronyak, R., Treusch, R., Kocharyan, V., Weckert, E., Wurth, W. & Vartanyants, I. A. (2013). *Phys. Rev. Lett.* **111**, 034802.
- Song, C. (2018). *IUCrJ*, **5**, 522–523.
- Song, C., Tono, K., Park, J., Ebisu, T., Kim, S., Shimada, H., Kim, S., Gallagher-Jones, M., Nam, D., Sato, T., Togashi, T., Ogawa, K., Joti, Y., Kameshima, T., Ono, S., Hatsui, T., Iwata, S., Yabashi, M. & Ishikawa, T. (2014). *J. Appl. Cryst.* **47**, 188–197.
- Tamasaku, K., Shigemasa, E., Inubushi, Y., Katayama, T., Sawada, K., Yumoto, H., Ohashi, H., Mimura, H., Yabashi, M., Yamauchi, K. & Ishikawa, T. (2014). *Nat. Photon.* **8**, 313–316.
- Tanaka, T., Kato, M., Saito, N., Owada, S., Tono, K., Yabashi, M. & Ishikawa, T. (2017). *Opt. Lett.* **42**, 4776–4779.
- Tono, K., Togashi, T., Inubushi, Y., Sato, T., Katayama, T., Ogawa, K., Ohashi, H., Kimura, H., Takahashi, S., Takeshita, K., Tomizawa, H., Goto, S., Ishikawa, T. & Yabashi, M. (2013). *New J. Phys.* **15**, 083035.
- Vartanyants, I. A. & Singer, A. (2010). *New J. Phys.* **12**, 035004.
- Vartanyants, I. A., Singer, A., Mancuso, A. P., Yefanov, O. M., Sakdinawat, A., Liu, Y., Bang, E., Williams, G. J., Cadenazzi, G., Abbey, B., Sinn, H., Attwood, D., Nugent, K. A., Weckert, E., Wang, T., Zhu, D., Wu, B., Graves, C., Scherz, A., Turner, J. J., Schlotter, W. F., Messerschmidt, M., Lüning, J., Acremann, Y., Heimann, P., Mancini, D. C., Joshi, V., Krzywinski, J., Soufli, R., Fernandez-Perea, M., Hau-Riege, S., Peele, A. G., Feng, Y., Krupin, O., Moeller, S. & Wurth, W. (2011). *Phys. Rev. Lett.* **107**, 144801.
- Young, L., Kanter, E. P., Krässig, B., Li, Y., March, A. M., Pratt, S. T., Santra, R., Southworth, S. H., Rohringer, N., Dimauro, L. F., Doumy, G., Roedig, C. A., Berrah, N., Fang, L., Hoener, M., Bucksbaum, P. H., Cryan, J. P., Ghimire, S., Glowia, J. M., Reis, D. A., Bozek, J. D., Bostedt, C. & Messerschmidt, M. (2010). *Nature*, **466**, 56–61.
- Yumoto, H., Mimura, H., Koyama, T., Matsuyama, S., Tono, K., Togashi, T., Inubushi, Y., Sato, T., Tanaka, T., Kimura, T., Yokoyama, H., Kim, J., Sano, Y., Hachisu, Y., Yabashi, M., Ohashi, H., Ohmori, H., Ishikawa, T. & Yamauchi, K. (2013). *Nat. Photon.* **7**, 43–47.